Use of MODIS-derived surface reflectance data in the ORAC-AATSR aerosol retrieval algorithm: Impact of differences between sensor spectral response functions

Andrew M. Sayer [a,b,*], Gareth E. Thomas [a], Roy G. Grainger [a], Elisa Carboni [a],
Caroline Poulsen [b], Richard Siddans [b]

[a] Department of Physics, University of Oxford, Parks Road, Oxford, OX1 3PU, UK
[b] Science and Technology Facilities Council Rutherford Appleton Laboratory, Harwell Science and Innovation Campus, Didcot, OX11 0QX, UK

ARTICLE INFO

ABSTRACT

The aerosol component of the Oxford-Rutherford Appleton Laboratory (RAL) Aerosol and Clouds (ORAC) retrieval scheme for the Advanced Along-Track Scanning Radiometer (AATSR) uses data derived from the Moderate Resolution Imaging Spectroradiometer (MODIS) to constrain the brightness of the surface. However, the spectral response functions of the channels used (centred near 550 nm, 660 nm, 870 nm, and 1.6 μm) do not exactly match between the two sensors. It is shown that failure to account for differences between the instruments' spectral response functions leads to errors of typically 0.001–0.01 in spectral surface albedo, and distinct biases, dependent on wavelength and surface type. A technique based on singular value decomposition (SVD) is used to reduce these random errors by an average of 35% at 670 nm and over 60% at the other wavelengths used. The technique reduces the biases so that they are negligible. In principle, the method can be extended to any combination of sensors. The SVD-based scheme is applied to AATSR data from the month of July 2008 and found to increase the number of successful aerosol retrievals, the speed of retrieval convergence, and improve the level of consistency between the measurements and the retrieved state. Additionally, retrieved aerosol optical depth at 550 nm shows an improvement in correspondence when compared to Aerosol Robotic Network (AERONET) data.

© 2011 Elsevier Inc. All rights reserved.

1. Introduction

Satellite radiometers play an important role in the assessment of the global burden of atmospheric aerosols. This is of particular interest because the direct and indirect radiative effects of aerosol are among the least certain contributions to radiative forcing (Forster et al., 2007; Stevens & Feingold, 2009). Over the land and sun-glint or ice-covered regions of the ocean, a large proportion of the top-of-atmosphere (TOA) reflectance measured by such instruments in the visible and near-infrared arises from the reflectance of sunlight by the surface of the Earth. An accurate aerosol retrieval requires the disentanglement of the surface and atmospheric contributions to the measured signal. Hence good knowledge of the reflectance characteristics of the surface is necessary. However, measurements from current satellite sensors do not generally have sufficient information content to unambiguously retrieve aerosol microphysical properties and the spectral and directional behaviour of the surface reflectance from a single overpass

(Hasekamp & Landgraf, 2007; Kokhanovsky et al., 2007, 2010); as a result, assumptions about aerosol and surface properties are necessary in aerosol retrieval algorithms (including, for example, Diner et al., 2005; Hsu et al., 2004; Levy et al., 2007; Martonchik et al., 1998; North, 2002; Thomas et al., 2009a, 2009b; Torres et al., 1998; Veefkind et al., 1998; von Hoyningen-Huene et al., 2002, 2003).

The Oxford-Rutherford Appleton Laboratory (RAL) Aerosol and Clouds (ORAC) retrieval scheme (Thomas et al., 2009a), applied to data from the Advanced Along-Track Scanning Radiometer (AATSR), performs a simultaneous retrieval of aerosol properties and surface reflectance. Surface reflectance data derived from the Moderate Resolution Imaging Spectroradiometers (MODIS, Schaaf et al., 2002) are used over land to fix the directional behaviour of the surface, and as an *a priori* value of the absolute brightness. However because MODIS and AATSR are different sensors it is important to account for the impact of their different spectral responses. The objective of this paper is to improve the algorithm by quantifying these differences and minimising this source of error. Section 2 provides an overview of relevant features of AATSR and ORAC, and Section 3 describes the improved treatment of land surface reflectance. Section 4 presents an updated retrieval error budget in light of the improved surface treatment. Section 5 shows the impact of the updated scheme on aerosol retrievals.

* Corresponding author at: Goddard Earth Sciences Technology and Research (GESTAR), NASA Goddard Space Flight Center, Greenbelt, MD 20771, USA. Tel.: +1 301 614 6211; fax: +1 301 614 6307.
E-mail address: andrew.sayer@nasa.gov (A.M. Sayer).

2. Overview of the ORAC-AATSR aerosol retrieval

Detailed descriptions of ORAC as applied to AATSR are provided by Sayer (2009) and Thomas et al. (2009a); a brief overview of relevant information is provided here. AATSR is aboard Envisat (launched March 2002) in a Sun-synchronous polar orbit with a mean local solar equatorial crossing time of 10 am for the descending node. The radiometer measures at seven channels in the visible and infrared, and the first four (centred near 550 nm, 660 nm, 870 nm and 1.6 μm) are currently used in the aerosol retrieval scheme. AATSR has an on-board visible calibration system; together with vicarious calibration against stable ground targets, this means that the random error on the solar channel radiances is 2–3% (Smith et al., 2008).

The area sampled by AATSR consists of two curved swathes approximately 550 km wide: a nadir view, looking down at zenith angles from 0°–22°, and a forward view inclined between 53° and 55° to the normal to the surface. The pixel size is 1 km × 1 km at nadir and approximately 1.5 km × 1.5 km at the centre of the forward swath; the level 1b product used colocates and regrids forward-view measurements to the nadir-view grid. The two views image the same ground scene with a time difference of about 150 s. The revisit period is 3–6 days, dependent on latitude. To improve computational speed, cloud-free forward and nadir-view data are typically averaged to a 10 km sinusoidal grid before the ORAC retrieval is performed (with the requirement that at least 50% of the input pixels are cloud-free). This averaging to a coarser resolution is known as 'superpixelling'. From here, the term 'ground scene' is taken to refer to the data, superpixelled or not, used for an individual retrieval.

ORAC is an Optimal Estimation (OE) retrieval (Rodgers, 2000), which aims to find the most probable state of the surface and atmosphere given measurements and *a priori* information on the state. The robust statistical basis of OE provides the following advantages:

1. Estimates of the quality of the retrieval solution (the retrieval 'cost') for each ground scene. This is essentially a weighted χ^2 test of the retrieval solution, and provides a level of confidence as to the results of any one retrieval.
2. Estimates of the random error on each retrieved parameter for each ground scene. These arise through knowledge of the uncertainty on the measurements and any *a priori* data, propagated through the forward model.
3. The ability (but not requirement) to use any *a priori* data available on the state parameters. The focus of the work presented in the next section is an improvement of the treatment of the MODIS land surface reflectance data used for the surface albedo *a priori* over land.

The shortwave quantity reported by AATSR for a given channel is an approximation of the spectral bidirectional reflection factor, the Sun-normalised radiance $R_{TOA}(\theta_s, \phi_s; \theta_v, \phi_v)$:

$$R_{TOA}(\theta_s, \phi_s; \theta_v, \phi_v) = \frac{\int_{\lambda_1}^{\lambda_2} \pi L_\lambda^r \varrho(\lambda) d\lambda}{\int_{\lambda_1}^{\lambda_2} \cos\theta_s E_\lambda^i \varrho(\lambda) d\lambda}. \quad (1)$$

In the above θ_s, ϕ_s denote the solar zenith and azimuth angles and θ_v, ϕ_v the corresponding angles of view (the AATSR sensor) respectively. A channel is defined between wavelengths λ_1, λ_2 to have response $\varrho(\lambda)$. Finally L_λ^r is the radiance measured by the instrument and E_λ^i is the TOA downward solar irradiance. The measurements used (the 'measurement vector') are the eight Sun-normalised radiances (four wavelengths at two viewing geometries).

The retrieved state parameters (the 'state vector') are the aerosol optical depth (AOD) at 550 nm (τ_{550}), the aerosol effective radius (r_{eff}), and the surface bihemispherical reflectance (BHR, Schaepman-Strub et al., 2006; also known as white-sky albedo) at each of the four wavelengths used ($R_{dd,1}$, $R_{dd,2}$, $R_{dd,3}$ and $R_{dd,4}$ for 550 nm, 660 nm,

870 nm, and 1.6 μm respectively). The wavelength of 550 nm is chosen for AOD as it is commonly used in the literature; the derived AOD may, however, be referenced to any wavelength desired, and is obtained from all measurements simultaneously. Both AOD and effective radius are retrieved in $\log_{10}$ space.

The retrieval is performed for a selection of five aerosol models, corresponding to typical continental, desert, maritime, urban, or biomass burning aerosol. These models consist of mixtures of aerosol components, and different effective radii are obtained by altering their mixing ratios during the retrieval. The first four models are drawn from the Optical Properties of Aerosols and Clouds (OPAC) database (Hess et al., 1998), while the biomass burning model is taken from Dubovik et al. (2002). Mie theory is used for all models except desert dust, which is treated as a mixture of spheroids (Table 6 of Kandler et al., 2007) for which T-Matrix code (Mishchenko & Travis, 1998) is used to calculate the phase function. A cost statistic under 10 indicates an acceptable consistency between the measurements and retrieved state, and is used as a threshold for a successful retrieval (Sayer et al., 2010). Generally the most likely aerosol type is taken as the one resulting in the lowest retrieval cost. However, this has been found to perform poorly over deserts, due to a lack of contrast between the surface and atmosphere. A modified scheme is therefore applied for deserts. Firstly, the retrieved BHR are used to calculate the (surface, not TOA) normalised difference vegetation index (NDVI) as follows:

$$NDVI = \frac{R_{dd,3} - R_{dd,2}}{R_{dd,3} + R_{dd,2}}. \quad (2)$$

Retrievals over land where 0 < NDVI < 0.25 are classified as deserts. In these cases the desert dust model is chosen (provided the cost is lower than 10). If the desert model has a cost larger than 10, the best aerosol type reverts to the lowest-cost model.

3. An improved treatment of land surface reflectance

3.1. Surface reflectance in the ORAC forward model

The ORAC forward model makes use of a bidirectional reflectance distribution function (BRDF, Schaepman-Strub et al., 2006) to describe the angular variation of the surface reflectance. This is a more realistic treatment than assuming a Lambertian surface. In the BRDF forward model, it is necessary to define three types of surface reflectance:

1. The surface bidirectional reflectance (the BRDF evaluated for the particular viewing geometry), R_{bb}. This describes the reflection of the direct solar beam into the viewing angle, and is a function of both solar and viewing angles.
2. The directional-hemispherical reflectance (DHR, also known as black-sky albedo), R_{bd}. This describes the isotropic reflection of the direct beam over the whole hemisphere (or alternatively direct reflection of incoming isotropic radiance), and is a function of the solar angle. The short time-delay between the forward and nadir views means that the solar angle and hence DHR are effectively identical for both views.
3. The BHR (white-sky albedo), R_{dd}. This describes the reflection of diffuse downwelling radiation, assumed isotropic, and so is independent of the geometry. This is the quantity retrieved in ORAC. In this work, the term 'surface albedo' refers to the BHR.

In this notation the subscript b indicates a direct beam and d a diffuse field; R_{bd}, for example, denotes an incoming direct beam being diffusely reflected.

Given an analytical description of the BRDF, the DHR for a given solar zenith angle may be obtained by integration over all satellite viewing zenith and relative (solar–satellite) azimuth angles. This may then be integrated over all solar angles to obtain the BHR. Because there is insufficient information to retrieve the full BRDF from the

AATSR measurements, BRDF models are used to generate R_{bb}, R_{bd} and the a priori R_{dd}. The ratios R_{bb}:R_{dd} and R_{bb}:R_{bd} are fixed in the aerosol retrieval, such that when R_{dd} is scaled in an iterative step in the retrieval then these ratios are used to scale R_{bb} and R_{bd} by the corresponding factor. Over land, the MODIS BRDF model parameters data product (MCD43B1) is used to define the shape of the BRDF and set the above ratios and the a priori DHR. The treatment over ocean, and some further information on surface reflectance in ORAC, is given by Sayer et al. (2010).

3.2. The MODIS BRDF product and forward model

The MODIS sensors are radiometers with a 2330 km swath width, measuring at 36 channels in the visible and infrared with a spatial resolution between 250 m and 1 km (dependent on channel). Two instruments are in orbit, one each on the NASA satellites Terra (10:30 am descending node time) and Aqua (1:30 pm ascending node). The MCD43B1 product (Schaaf et al., 2002) consists of a set of kernel weights for the Algorithm for MODIS Bidirectional Reflectance Anisotropy of the Land Surface (AMBRALS, Wanner et al., 1997) surface BRDF model. The model calculates bidirectional reflectance as a weighted sum of three kernels (detailed by Wanner et al., 1995), representing reflectance from different types of surface.

The weighting parameters are obtained at 1 km × 1 km spatial resolution grid by inversion of 16 days of cloud-free atmospherically-corrected reflectances from both MODIS instruments (Lucht et al., 2000). Collection 5 of the data, available every eight days, is used. Weights are obtained for seven MODIS solar channels (four of which are centred near AATSR channels) and three broad bands. To reduce the storage overhead, each MODIS data granule is down-sampled to approximately 2.5 km × 2.5 km resolution and the broadband datasets removed before processing in ORAC. In the version of ORAC described by Thomas et al. (2009a), the BRDF is obtained from the MCD43B1 product, and integrated to provide the DHR and BHR for a MODIS-like sensor using a precalculated lookup table of kernel integrals and an expression provided by Lucht et al. (2000) respectively. These 'MODIS-like' quantities are referred to as $R_{bb,M}$, $R_{bd,M}$ and $R_{dd,M}$ (with the subscript M indicating MODIS).

3.3. Adaptation to AATSR channels

MODIS and AATSR are different sensors and each channel measures not a single wavelength but a narrow band. As a result, the surface albedo reported by MODIS is an average albedo over the band, weighted by the instrument's response function. Fig. 1 shows that the visible channel response functions for the two instruments do not match, so if the true spectral surface albedo varies across each band, then the surface albedo each instrument would see for the same underlying surface would differ. This effect would be the most pronounced for the 660 nm and 1.6 μm channels, as these have the least similar response functions between the two instruments. In this work the magnitude of the error that use of MODIS data introduces is quantified, and reduced through correction of the MODIS product.

3.3.1. High-resolution spectral databases

The Advanced Spaceborne Thermal Emission and Reflection Radiometer (ASTER, Baldridge et al., 2009) and United States Geological Survey (USGS, Clark et al., 2003) spectral libraries provide high-resolution data on the reflectance of a large variety of natural and man-made substances from laboratory measurements. A selection of 51 spectra from the ASTER library and 100 from the USGS library, chosen as representatives of surfaces that are found on the Earth's surface (such as various types of vegetation; sand and soil; snow, ice and frost; or man-made substances such as concrete), are used here to quantify the impact of the visible channel shapes shown in Fig. 1 on the MODIS-reported BHR as compared to AATSR. This requires the following assumptions:

1. The spectra chosen are representative of the spectra of surfaces that make up the Earth's surface.
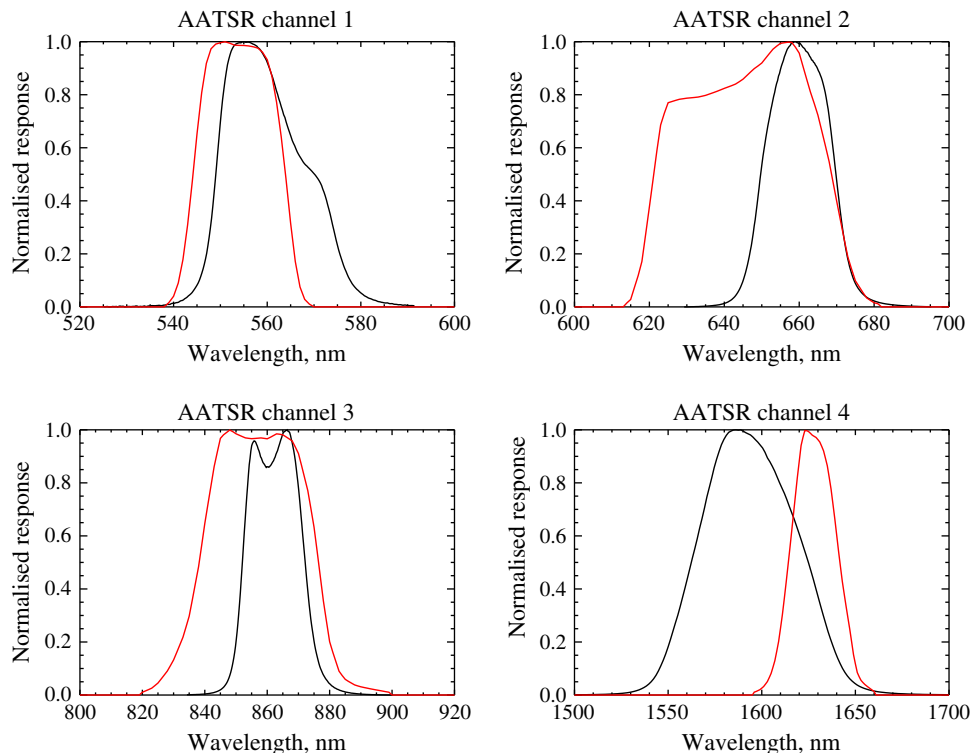

Fig. 1. AATSR (black) and MODIS (red) normalised visible channel response functions. MODIS channels closest to corresponding AATSR channels are shown.

2. The difference found between integration of the spectra over the instruments' visible channel response functions can be related to differences between MODIS and AATSR surface albedos (as the spectra lack directional information), and any correction applied to the $R_{dd, M}$ to estimate R_{dd} can then also be applied to $R_{bb,M}$ and $R_{bd,M}$ to obtain R_{bb} and R_{bd}.

These spectra are grouped according to the type of surface that they represent: 35 soils, 6 sands, 8 man-made substances, 4 spectra of snow, ice or frost and 104 assorted types of vegetation. Convolving these spectra with the instruments' visible channel response functions leads to a set of 157 pairs of simulated 'observed' surface albedos for MODIS ($R_{dd,M}$) and AATSR (R_{dd}). The differences between surface albedo reported from MODIS and AATSR calculated for these spectra are shown as a function of the AATSR 'observed' albedo in Fig. 2. The MODIS-AATSR difference $R_{dd,M} - R_{dd}$ is hereafter referred to as the 'expected difference', ϵ_e. The largest departures, as suggested by Fig. 1, are for 660 nm and 1.6 μm, with a clear bias particularly visible at 1.6 μm. The mean absolute differences in Fig. 2 are 0.0034 at 550 nm, 0.0057 at 660 nm, 0.0015 at 870 nm and 0.012 at 1.6 μm.

3.3.2. Singular value decomposition of spectrally-derived albedo

Singular value decomposition (SVD) is a statistical tool that may be applied to describe the variability in a set of data; in this case it is applied to allow the prediction of an AATSR-observed albedo for a scene given that observed by MODIS. The technique described here can, in principle, be applied to any combination of sensors. The SVD of an m-by-n matrix $\mathbf{M}$ is defined as follows:

$$\mathbf{M} = \mathbf{U}\Sigma\mathbf{V}^*. \tag{3}$$

This states that $\mathbf{M}$ may be expressed as a product of three matrices: $\mathbf{U}$ is an m-by-m unitary matrix, $\mathbf{V}^*$ an n-by-n unitary matrix, and the

matrix Σ is an m-by-n diagonal matrix with the nonzero elements in descending order. The conjugate transpose of $\mathbf{V}^*$, $\mathbf{V}$, is the matrix of interest here as it describes the patterns of the variability in $\mathbf{M}$. In this case $\mathbf{V}^*$ does not have imaginary components and so is equivalent to the transpose matrix $\mathbf{V}^T$. $\mathbf{U}$ contains a set of basis vectors which can be used to describe $\mathbf{M}$. The columns of $\mathbf{U}$ and $\mathbf{V}$ are known as singular vectors. The elements of Σ, known as the singular values, describe how important each singular vector $\mathbf{v}$ in $\mathbf{V}$ is to the variability in $\mathbf{M}$: the contribution of a singular vector in $\mathbf{V}$ to the total variability is its corresponding singular value as a proportion of the total of the singular values. Hence the first singular vector contains the most information on the variability.

The matrix $\mathbf{M}$ in this context consists of the simulated surface albedos reported by MODIS and AATSR for each spectrum; hence, it has one column for each spectrum used (157) and one row for each instrument channel. Results are discussed using the 4 AATSR channels and their equivalent MODIS bands (for a total of 8 rows). In this discussion n_M refers to the number of MODIS bands used, and n_A the number of AATSR bands (4 in both cases).

The calculations described were also performed using the three additional MODIS bands centred at 460 nm, 1.2 μm and 2.2 μm (i.e. $n_M = 7$ and a total of 11 rows in $\mathbf{M}$). Including the additional three bands increases the data storage overhead of ORAC, and provides only negligible improvement on the $n_M = 4$ case. Therefore only the case of $n_M = 4$ is discussed further.

3.3.3. SVD fitting and $\tilde{R}_{dd}$ calculation

After computing the SVD as described above, the singular vectors $\mathbf{v}$ may be obtained. These can be used to make an estimate $\tilde{R}_{dd}$ of the AATSR surface albedo R_{dd} given the MODIS surface albedo $R_{dd, M}$ at each wavelength, for any spectrum contained within $\mathbf{M}$.

First, a simultaneous linear fit of the first n_M elements of each singular vector $\mathbf{v}_i$ (elements referred to as $\mathbf{v}_{i, M}$) to the n_M MODIS
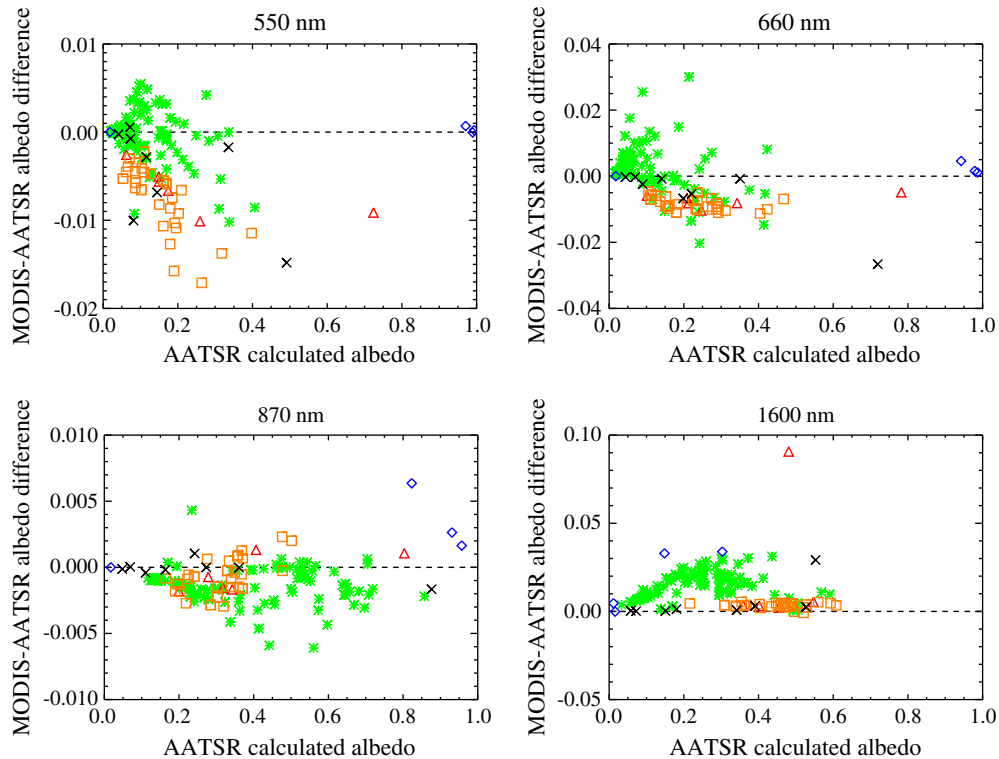
Fig. 2. Expected differences ϵ_e between surface albedo reported by MODIS and AATSR as calculated for the 157 spectra selected from the ASTER/USGS libraries, for bands corresponding to AATSR visible channels, as a function of albedo calculated for AATSR. Green stars are vegetation, red triangles sand, orange squares soil, blue diamonds snow or ice and black crosses man-made substances. Note the difference in axis scales between wavelengths.

surface albedos $R_{dd, M}$ in question is performed. These elements of $\mathbf{v}$ describe the variability in the MODIS channels. This yields a series of n_M coefficients, c_i, such that the MODIS surface albedo (at all n_M wavelengths) can be calculated exactly as the following:

$$R_{dd,M(1,2,\dots,n_M)} = \sum_{i=1}^{n_M} c_i \mathbf{v}_{i,M}. \tag{4}$$

Next, these coefficients are used to estimate the n_A AATSR surface albedos using the same summation, but with the last n_A elements of the singular vectors (referred to as $\mathbf{v}_{i,A}$) instead of the first n_M. These describe the variability in the AATSR channels, and lead to the following prediction of the value of the AATSR surface albedo at all n_A wavelengths:

$$\tilde{R}_{dd(1,2,\dots,n_A)} = \sum_{i=1}^{n_M} c_i \mathbf{v}_{i,A}. \tag{5}$$

The more singular vectors used, the greater the proportion of the variability in the spectra will be captured by them and so the more accurate the prediction $\tilde{R}_{dd}$ of R_{dd}. A maximum of n_M singular vectors may be used; any more and the fit of $R_{dd,M}$ described above will have non-unique solutions. In practice, four singular vectors will be used with four input MODIS surface albedos to provide four coefficients respectively to fit the AATSR-reported spectral surface albedo. If all eight singular vectors were used then $\mathbf{M}$ would be reconstructed perfectly, but the values of the AATSR surface albedo would be needed in the input to fit the data and so there would be no predictive power. Hence there is a trade-off between the number of values which can be predicted, and the accuracy of the predictions which can be made.

The first four singular vectors capture 99.3% of the variability in the spectra, suggesting that the fitting process described above should reconstruct the AATSR surface albedos well. The singular vectors obtained are tabulated in Table 1, together with their singular values; the similarity between elements corresponding to equivalent channels is an indication of the fact that the channels are generally observing similar surface albedos.

3.3.4. Quality of SVD fit

The value of the fit and estimation process can be quantified by comparing the error in the AATSR albedo that would result from using the MODIS albedo as an estimate (the 'expected difference' ϵ_e, defined previously) to the error resulting from using the SVD-predicted estimate, $\tilde{R}_{dd} - R_{dd}$. This second quantity is referred to as the 'AATSR reconstruction error' ϵ_r: if $|\epsilon_r| < |\epsilon_e|$ then the SVD fit provides an improved estimate of R_{dd} compared with using just the MODIS value directly.

Plots of $|\epsilon_e|$ against $|\epsilon_r|$ are shown in Fig. 3. For all classes of surface, the mean value of $|\epsilon_r|$ is smaller than the mean of $|\epsilon_e|$, although for a few individual cases the unadjusted MODIS-like surface albedo is a

Table 1
Values of the first four singular vectors (given here to three significant figures) obtained in the analysis of spectra, for $n_M = 4$ and $n_A = 4$. Singular vectors are numbered in order of their significance (with 1 being most significant). The final row gives the corresponding singular value for each singular vector.

Element detailing visible channel	Singular vector			
	1	2	3	4
MODIS 550 nm	−0.227	0.411	−0.0222	0.551
MODIS 660 nm	−0.248	0.435	0.210	−0.371
MODIS 870 nm	−0.497	−0.151	−0.466	−0.108
MODIS 1.6 μm	−0.379	−0.344	0.466	0.119
AATSR 550 nm	−0.230	0.413	−0.00414	0.496
AATSR 660 nm	−0.250	0.437	0.240	−0.510
AATSR 870 nm	−0.498	−0.156	−0.466	−0.109
AATSR 1.6 μm	−0.364	−0.338	0.497	0.117
Singular value	10.1348	2.89675	2.30584	0.372477

better match than the SVD-adjusted surface albedo. The mean values of $|\epsilon_r|$ are 0.0011 at 550 nm, 0.0021 at 660 nm, 0.00097 at 870 nm and 0.0044 at 1.6 μm. These mean absolute values of ϵ_e and ϵ_r are denoted σ_e and σ_r respectively, and so represent the magnitude of the error arising from sensor characteristics before and after making the SVD-based correction.

Fig. 4 shows the reconstruction errors ϵ_r as a function of the 'true' AATSR-observed surface albedo R_{dd}. A comparison with Fig. 2 shows that the use of singular vectors gives reconstruction errors with smaller overall biases (particularly at 1.6 μm) and less clustering of similar spectral types than direct use of the MODIS data. In summary, the use of SVD techniques generally allows an improved prediction of the AATSR BHR for a surface as compared to using the BHR derived from a MODIS-like sensor as-is.

3.3.5. Composite spectra

As the Earth's surface on a satellite pixel scale is unlikely to conform exactly to an individual spectrum present in the libraries used, it is important to quantify how well the singular vectors in Table 1 can predict R_{dd} for surfaces consisting of a composite of these spectra. Generation of an ensemble of a million composite spectra, each calculated from a linear combination of between 2 and 4 randomly-weighted and randomly-picked spectra, yields an ensemble of a million matched sets of R_{dd} and $R_{dd, M}$. From there, distributions of ϵ_e and ϵ_r are calculated after making the SVD fit; a million ensemble members ensures statistics robust to 2 significant figures.

Except at 1.6 μm, the mean absolute expected differences (σ_e) for the ensemble of composite spectra are smaller than the corresponding values for the group of 157 single spectra. This suggests that to some extent the impact of the differences between MODIS and AATSR is cancelled out by the different materials in the composite spectra. These values of σ_e are 0.0031 at 550 nm, 0.0041 at 660 nm, 0.0012 at 870 nm and 0.012 at 1.6 μm. The SVD technique proves effective in the case of composite spectra; σ_r are 0.00086 at 550 nm, 0.0015 at 660 nm, 0.00066 at 870 nm and 0.0034 at 1.6 μm.

Similar results are obtained if the number of spectra in each composite spectrum is changed (such as allowing 2–6 spectra rather than 2–4); the higher the maximum number of spectra allowed, the smaller the expected differences and reconstruction errors. The ratio of σ_r to σ_e remains similar. These results indicate that the technique also performs well for mixed spectra, such as are likely to be found for the Earth's surface.

3.3.6. Application to the retrieval

In the preprocessing of the aerosol retrieval $R_{bb,M}$, $R_{bd,M}$ and $R_{dd,M}$ are obtained from the MOD43B1 product for each ($1 \text{ km} \times 1 \text{ km}$) AATSR pixel. The singular vectors obtained from the 157 spectra are used to calculate $\tilde{R}_{dd}$, which is used as the a priori value of R_{dd} in the retrieval. The ratio $\tilde{R}_{dd} : R_{dd,M}$ is calculated for each pixel and then applied as a scaling factor to $R_{bb, M}$ and $R_{bd, M}$ to obtain R_{bb} and R_{bd}. This preserves the ratio between the three reflectances obtained from the MCD43B1 product. If the AATSR data are being superpixelled to a lower resolution (Section 2) the MODIS data within each superpixel are then averaged to give the mean R_{bb}, R_{bd} and R_{dd} used to initialise the retrieval for that ground scene. If for any wavelength the ratio $\tilde{R}_{dd} : R_{dd,M}$ is larger than 1.5 or smaller than 0.5, then it is deemed a poor fit of the singular vectors and no adjustment is made. This constraint helps to prevent unphysical estimates of R_{bb}, R_{bd} and R_{dd}.
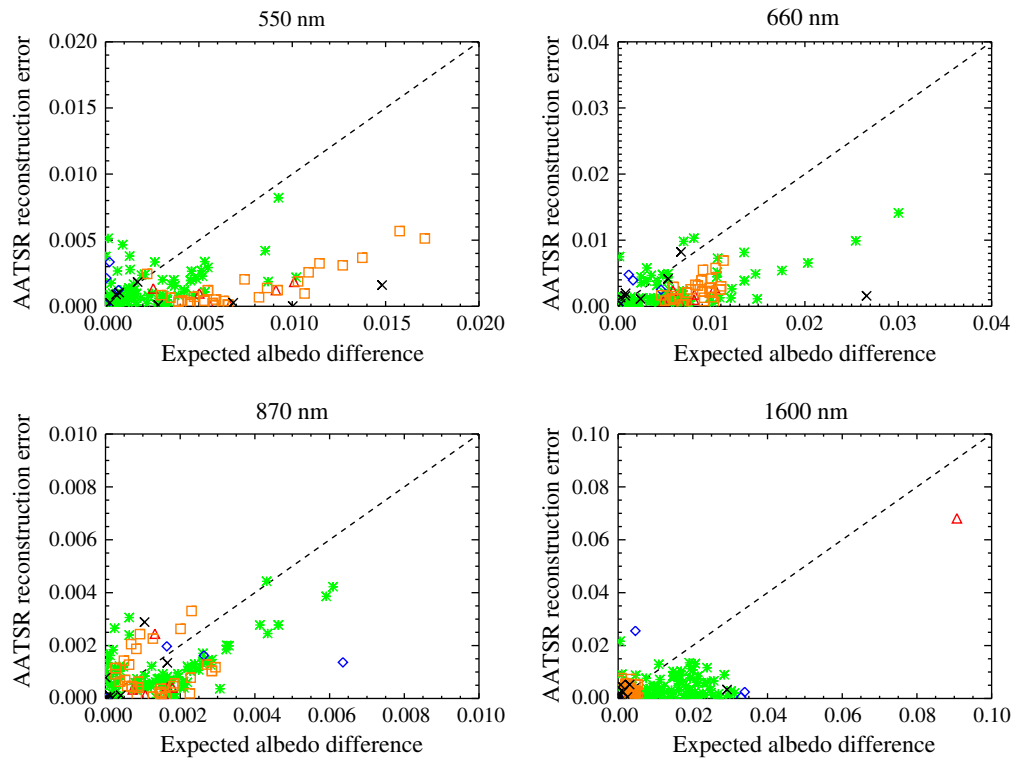
An example of this in practice is shown in Fig. 5. Well-defined areas of differing land surface cover result in adjustments made to $R_{dd, M}$ of differing signs and magnitudes, with a strong agreement between the sign of the adjustment and the reverse of the sign of the expected MODIS-AATSR difference for spectra in different categories (such as vegetation, sand and soil) shown in Fig. 2.

Histograms of the magnitude of the adjustment for this scene are presented in Fig. 6; the wavelength-dependence of the magnitude of the

Fig. 3. Expected difference in surface albedo ϵ_e against reconstruction error ϵ_r for the 157 spectra used in the analysis, at AATSR visible channel wavelengths. Presented in units of absolute albedo, using 4 MODIS channels and singular vectors. Green stars are vegetation, red triangles sand, orange squares soil, blue diamonds snow or ice and black crosses man-made substances. Note the difference in axis scales between wavelengths.

adjustment (smaller at 550 nm and 870 nm, larger at 660 nm and 1.6 μm) is also consistent with the single-spectrum results. Additionally, the means of the distribution of adjustments for this scene and in the

ensemble of composite spectra from Section 3.3.5 are similar: they would not be expected to match exactly, as the mean of the scene depends upon the composition of the land surfaces in it, but the
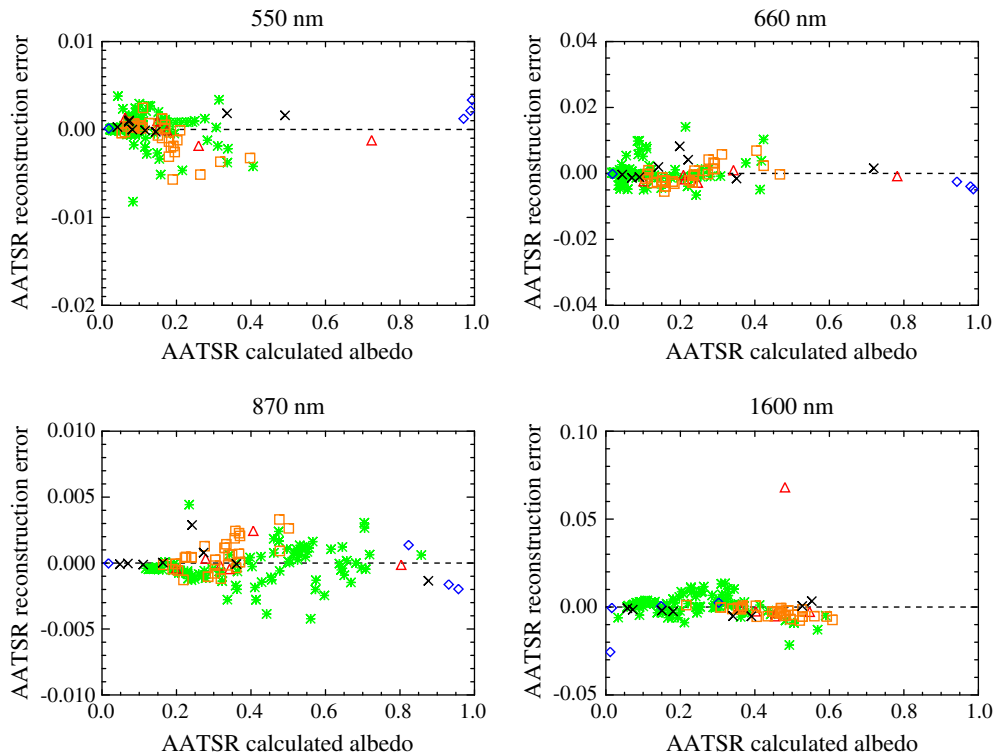
Fig. 4. AATSR-observed surface albedo against reconstruction error for the 157 spectra used in the analysis, at AATSR visible channel wavelengths. Green stars are vegetation, red triangles sand, orange squares soil, blue diamonds snow or ice and black crosses man-made substances.
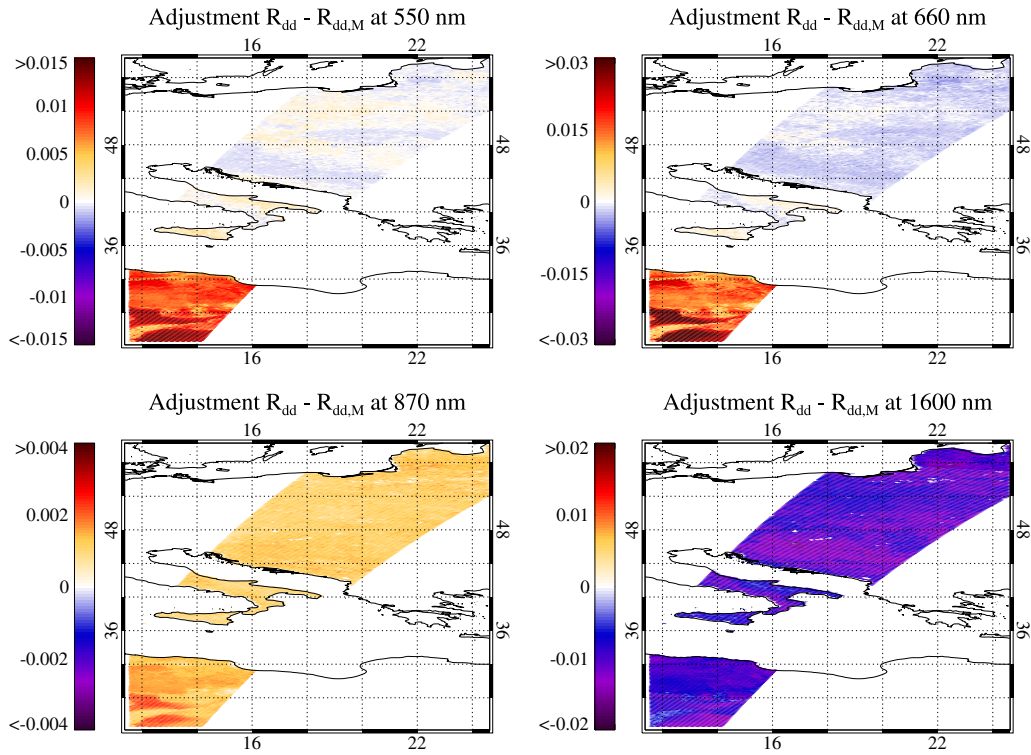
Fig. 5. Adjustment $R_{dd} - R_{dd, M}$ made to the MODIS white-sky surface albedo at AATSR visible channel wavelengths, in units of absolute albedo. The scene covers continental Europe and parts of Northern Africa for an AATSR swath on September 5, 2004.

similarity suggests that the spectra provide a reasonable representation of land surfaces. Together these figures provide confidence that the method, which was shown in earlier sections to provide results valid for individual and composite spectra, also yields physically reasonable estimates of the AATSR BHR when applied to real MCD43B1 data.

4. Revised retrieval error budget

The ability of OE to provide meaningful information on the consistency between measurements and the retrieved state, and estimates of the uncertainty on retrieved parameters, is contingent on knowing accurately the uncertainties associated with the measurements, forward model, and *a priori* data. In ORAC, these are described

Fig. 6. Frequency histograms of the magnitude of the adjustment $|R_{dd} - R_{dd, M}|$ made to the MODIS white-sky surface albedo at AATSR visible channel wavelengths for the scene shown in Fig. 5. Presented in units of absolute albedo. The bin size for density calculations is 0.0001. Black indicates data for 550 nm, red 660 nm, green 870 nm and blue 1.6 μm. The dashed-dotted lines indicates the mean of the distribution for each wavelength as indicated by their colours, and dashed lines the mean adjustment of the ensemble of a million composite spectra discussed in Section 3.3.5.

by the covariance matrices $\mathbf{S}_a$ (*a priori* state uncertainty) and $\mathbf{S}_y$ (the combination of measurement and forward model uncertainty); more details are provided by Rodgers (2000), Sayer (2009), Sayer et al. (2010) and Thomas et al. (2009a). In these matrices the value of element index i, j is the product of the uncertainties on measurements or parameters i and j and the correlation between them. The revised surface treatment necessitates an update to these matrices.

4.1. The a priori uncertainty on surface albedo

The components of $\mathbf{S}_a$ relating to AOD and effective radius are detailed by Sayer (2009) and Thomas et al. (2009b) and are unchanged here. The following sources of uncertainty are considered to calculate the terms related to surface albedo:
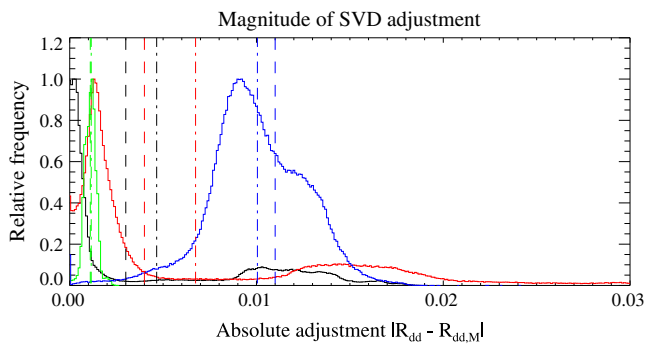
1. Remaining differences due to sensor characteristics after the SVD fit (the reconstruction error).
2. Random errors in the MCD43B1 data product.
3. Temporal variability of surface albedo arising from the use of 8-daily rather than instantaneous MCD43B1 data.

4.1.1. The reconstruction error

Section 3.3.4 shows that although the SVD adjustment technique can account for much of the difference between MODIS-like and AATSR-like sensors, the 'true' surface albedo that AATSR would see is not perfectly reconstructed. Therefore the mean absolute reconstruction errors σ_r of 0.0011 at 550 nm, 0.0021 at 660 nm, 0.00097 at 870 nm and 0.0044 at 1.6 μm contribute to the uncertainty on the *a priori* BHR. These are taken to be uncorrelated between wavelengths.

4.1.2. Errors in the MCD43B1 parameters

The MCD43B1 dataset is a retrieved product and hence has some associated error. Although several studies have examined various aspects of the model parameters and derived (mainly broadband) albedo (Jin et al., 2003a, 2003b; Liu et al., 2009; Saloman et al., 2006;

Shuai et al., 2010 and others) and found performance to be generally as expected, there has been no published global systematic validation of the Collection 5 spectral white-sky albedo dataset. Hence, the contribution of errors in the MODIS data to the *a priori* covariance matrix is taken to be 10% of the BHR, to a minimum of 0.005 (C. Schaaf, personal communication, 2009).

As $R_{dd, M}$ is calculated at full (1 km × 1 km) AATSR instrumental resolution in ORAC, the correlation coefficients $r_{(i, j)}$ of $R_{dd, M}$ between pairs of wavelengths i and j can be determined for each ground scene. This 10% error in $R_{dd, M}$ is assumed to be correlated between wavelengths according to these correlation coefficients. If fewer than 10 unique MODIS values are found in a ground scene (because of, for example, missing MODIS data due to cloud cover, or the ORAC retrieval being performed at full AATSR resolution) then the correlations are set to zero.

4.1.3. Temporal variability

Processes such as the growth, flowering or death of plants and the falling of rain or snow (or drying following precipitation) may change the surface albedo on timescales shorter than the 8-day period at which the MCD43B1 product is available. Therefore some additional error term is included to account for this. A simple scheme for the temporal variability of albedo has been developed by Ward (2009). This involved the examination of time-series of surface albedo reported by MODIS of selected homogeneous 10 km × 10 km regions from different surface cover types. For each region, the magnitude of the temporal variability of the surface albedo on these timescales was estimated by comparing the difference between surface albedo for successive 8-day periods with the standard error (standard deviation divided by the square root of the number of 1 km × 1 km pixels) on each estimate of surface albedo for the 10 km × 10 km area.

The analysis produced estimates of the typical temporal variability of BHR for three classifications of surface. Firstly, a snow index is calculated based on the BHR at 550 nm and 1600 nm:

$$\frac{R_{dd,1} - R_{dd,4}}{R_{dd,1} + R_{dd,4}}. \tag{6}$$

If this snow index is larger than 0.4 then the ground scene is classified as snowy and the temporal variability contributions to the *a priori* error are 0.0168 at 550 nm, 0.0204 at 660 nm, 0.0259 at 870 nm and 0.0146 at 1600 nm. If the conditions for the snow test are not satisfied, then the surface NDVI (Eq. (2)) is calculated. For NDVI>0.3 the ground scene is classified as vegetated and the temporal variability contributions to the *a priori* error are 0.0075 at 550 nm, 0.0081 at 660 nm, 0.0113 at 870 nm and 0.0112 at 1600 nm. If the ground scene meets neither the snowy criterion nor the vegetated criterion, then it is classified as bare and the temporal variability contributions to the *a priori* error are 0.0019 at 550 nm, 0.0023 at 660 nm, 0.0030 at 870 nm and 0.0039 at 1600 nm. These values are generally larger than the reconstruction error σ_r.

In all cases, these temporal variability contributions to the *a priori* uncertainty are assumed to be uncorrelated between wavelengths, because the correlations observed by Ward (2009) were highly variable for different regions. In the case of a severe change in surface cover (such as snowfall or snow melt) these uncertainties may drastically underestimate the temporal variability of albedo, and the changes in albedo may in fact be strongly correlated. In such cases (such as an AATSR orbit just after heavy snowfall for a scene which was otherwise snow-free for the majority of the MODIS overpasses) the aerosol retrieval is likely to fail as the surface reflectance is constrained too far away from the true value. Use of a MODIS-independent snow mask for AATSR such as that recently developed by Istomina et al. (2010) would be of utility in these situations. However, as snow-covered land scenes are often identified as cloudy by the AATSR cloud flag, and the number of scenes affected by sudden snowfall or melt is small, the number of affected potential retrievals is low (although this may be significant in some regions and seasons).

4.1.4. Combination of errors

The total uncertainty on the *a priori* R_{dd} is taken as being the sum of the three contributions described above; these are assumed to be independent of each other, and so are added in quadrature:

$$\mathbf{S}_{a(i,j)} = \sigma_{r(i)}\sigma_{r(j)}\delta_{(i,j)} + \sigma_{t(i)}\sigma_{t(j)}\delta_{(i,j)} + \sigma_{R_{dd,M(i)}}\sigma_{R_{dd,M(j)}}r_{i,j}. \tag{7}$$

In the above $\mathbf{S}_{a(i,j)}$ represents the covariance matrix element i, j, with σ_r the reconstruction errors, σ_t the temporal variability and $\sigma_{R_{dd, M}}$ the (10% to a minimum of 0.005) uncertainty on the MODIS BHR. The Kronecker delta $\delta_{(i,j)}$ indicates these first two terms are uncorrelated between wavelengths i and j while $r_{i,j}$ allows for correlated error in the MODIS-returned surface albedo.

For bright surfaces and long wavelengths, the dominant contribution comes from the retrieval error on the MODIS surface albedo. However, at short wavelengths, and particularly for vegetated surfaces, all terms of the error budget are important. As aerosols also tend to be more optically active at shorter wavelengths, accurate characterisation of the surface reflectance at these wavelengths is of particular importance. As well as decreasing the total uncertainty on the *a priori* surface albedo (as $\sigma_r < \sigma_e$), the SVD technique substantially decreases the biases inherent as a result of the differing sensors' spectral response functions.

4.2. Forward model parameter uncertainty

The covariance matrix $\mathbf{S}_y$ details the precision with which the retrieval is expected to be able to fit the measurements. This includes contributions from the random error on the measurements, numerical error in the retrieval forward model, and the impact of fixed forward model parameters (in this case, the fixed ratios $R_{bb}:R_{dd}$ and $R_{bb}:R_{bd}$). Details of the calculation of each of these terms are given by Sayer (2009); however, the estimated forward model parameter uncertainty was calculated assuming the error in MODIS surface albedo products was 0.02 (the quoted accuracy of the broadband surface albedo), rather than the 10% value discussed in the previous section. Revised values are given in Table 2; these are of similar magnitude to the random error on the measurements (Smith et al., 2008) and are smaller for the forward view due to its longer atmospheric path length.

4.3. Retrieval averaging kernels

The averaging kernel $\mathbf{A}$ in the context of OE describes the rate of change of the retrieved state with respect to the true state, and is calculated (Rodgers, 2000) as
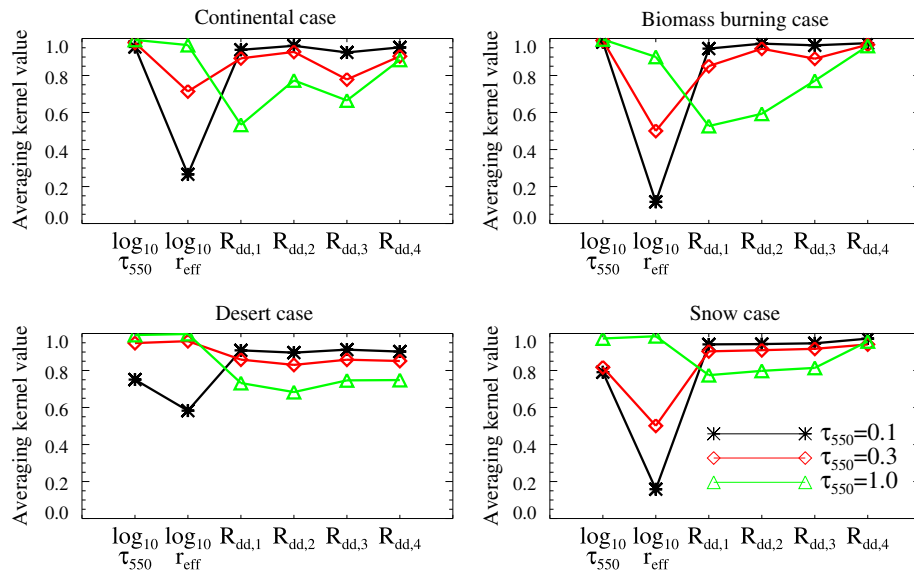
$$\mathbf{A} = \left(\mathbf{S}_a^{-1} + \mathbf{K}\mathbf{S}_y^{-1}\mathbf{K}^T\right)^{-1}\mathbf{K}\mathbf{S}_y^{-1}\mathbf{K}^T \tag{8}$$

Table 2
Forward model uncertainty in TOA reflectance over land arising from incorrect model parameters (the fixed ratios $R_{bb}:R_{dd}$ and $R_{bb}:R_{bd}$). Values are given as percentages of the measured TOA reflectance.

Channel	Nadir-view	Forward-view
	Error, %	Error, %
550 nm	1.61	1.19
660 nm	2.25	1.74
870 nm	2.97	2.79
1.6 μm	3.71	3.45

Fig. 7. Diagonal elements of averaging kernels for each of the four cases. State vector elements are indicated along the x-axis (logarithms of aerosol optical depth and effective radius, then spectral BHR). Clockwise from top left, results show continental aerosol over vegetated ground; biomass burning aerosol over dense vegetation; continental aerosol over snow; and dust aerosol over a desert. Black stars show results for an AOD at 550 nm of 0.1, red diamonds an AOD of 0.3, and green triangles an AOD of 1.

where $\mathbf{K}$ is the weighting function (also called Jacobian) matrix, i.e. the rate of change of the measurement vector with respect to the retrieved state. It can be seen that as the elements of $\mathbf{S}_a$ become larger (the *a priori* information becomes a weaker constraint), $\mathbf{A}$ tends towards the identity matrix. The diagonal elements of $\mathbf{A}$ thus describe how strongly the corresponding retrieved state vector element is influenced by the *a priori* data (with a value of 1 indicating that the retrieved state vector element is wholly determined by the measurements, and 0 indicating that the measurements provide no improvement on the *a priori* knowledge). Off-diagonal elements indicate a sensitivity of the particular state vector element to a change in a different state vector element. The trace of $\mathbf{A}$ provides the degrees of freedom for signal, the number of pieces of state information added by the measurements.

In general, $\mathbf{A}$ is a complicated function of the true state. Calculations are therefore presented here for a range of series of conditions: four surface cover and aerosol types (continental aerosol over a vegetated surface; biomass burning aerosol over a densely-vegetated surface; dust aerosol over a desert surface; and continental aerosol over a snow surface) at each of three aerosol loadings ($\tau_{550} = 0.1$, 0.3, 1.0). The aerosol microphysical properties are those used in the ORAC retrieval and the effective radii the *a priori* values for the relevant aerosol model. Information on these, and the calculation of $\mathbf{S}_y$ and $\mathbf{S}_a$, is provided in Sayer (2009) and Thomas et al. (2009a), or this work. Each surface is modelled as a Lambertian reflector with spectral BHR ($R_{dd,1}$, $R_{dd,2}$, $R_{dd,3}$ and $R_{dd,4}$ respectively) of 0.06, 0.08, 0.3, 0.2 for the vegetated case; 0.05, 0.05, 0.35, 0.15 for the densely-vegetated case; 0.25, 0.45, 0.55, 0.65 for the desert case; and 0.95, 0.96, 0.9, 0.15 for the snow case. These values have been chosen as typical for different surface cover types and the results are similar if

surface reflectances of similar magnitudes, or reasonable BRDF models, are used instead. Finally, the solar zenith angle is taken as 45°, satellite zenith angles 5° and 55° for nadir and forward views, and relative azimuth angles 45° and 90° for nadir and forward views.

Diagonal elements of the averaging kernels for these cases are shown in Fig. 7. Similar patterns are observed for all cases. The element relating to the AOD is very close to 1 for both of the vegetated cases, indicating the algorithm should be able to retrieve the AOD well; over the brighter desert and snow surfaces, the value is lower (around 0.8 for an aerosol loading of 0.1), due to a small contribution from the aerosol to TOA reflectance, but increases as aerosol loading increases. The effective radius is comparatively poorly-constrained by the measurements with a strong contribution from the *a priori* for all cases, although the situation improves for higher aerosol loadings. This indicates that retrievals of effective radius, and information derived using this, such as Ångström exponent, are likely less reliable than τ_{550}. Averaging kernel elements relating to BHR are very close to 1 for low aerosol loadings (as the majority of the TOA reflectance will arise from

Table 3
Comparison between aerosol retrievals using the new SVD-based land surface reflectance ('SVD') treatment with the previous land surface reflectance treatment ('unadjusted'). RMS indicates the root mean square difference.

Retrieved/derived parameter	Correlation coefficient r	RMS difference	Mean difference (SVD-unadjusted)
AOD (550 nm)	0.920	0.120	−0.032
Effective radius (μm)	0.631	0.545	0.088
AOD (870 nm)	0.883	0.110	−0.015
Ångström exponent	0.763	0.514	−0.207
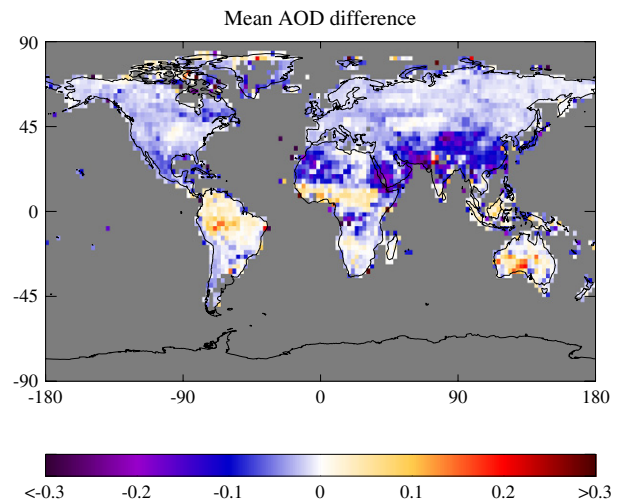
Fig. 8. Mean difference in retrieved 550 nm AOD (SVD-unadjusted) for those retrievals where both surface treatments are successful, averaged to a 25° grid. Grid cells without matched retrievals are indicated in grey.
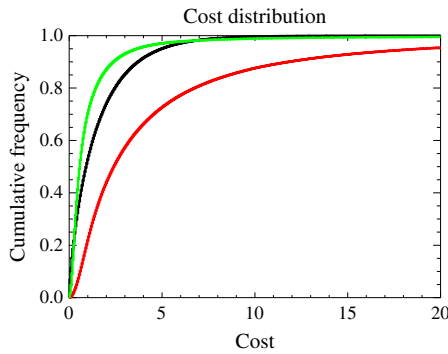
Fig. 9. Cumulative frequency distribution of retrieval cost for the unadjusted (red line) and SVD (green line) cases. The black line shows the theoretical result for a χ^2 distribution with 1.5 degrees of freedom.

direct reflection of solar radiation from the surface) and decrease as aerosol loading increases. The total degrees of freedom for signal is approximately 5 in all cases; as the aerosol loading increases, the measurements provide more information on τ_{550} and r_{eff} and less on the surface BHR. Off-diagonal elements are generally small, except those relating to effective radius at low (0.1) and moderate (0.3) AODs.

5. Impact on aerosol retrieval

To illustrate the impact of the new surface treatment on the aerosol retrieval scheme, the improved algorithm has been applied to AATSR data from the month of July 2008 (a total of 411 processed orbits). For comparison, the month has also been processed with the previous version of the algorithm. This control version uses the

MCD43B1 product directly (i.e. no SVD-based adjustment), and the previous error budget (i.e. a priori error of 0.02 on the BHR, no other contributions to $\mathbf{S}_a$ and no contribution from forward model parameter uncertainty to $\mathbf{S}_y$). These two datasets are referred to as the 'SVD' and 'unadjusted' runs respectively. Discussion in this section refers only to retrievals over land.

Table 3 shows statistics comparing those retrievals where convergence with cost under 10 was obtained for both the SVD and unadjusted runs. Overall the AOD at 550 nm is highly correlated (Pearson's linear correlation coefficient $r = 0.920$) with the SVD-based treatment resulting in an AOD lower on average by 0.032. The retrieved effective radius is less well-correlated (with the new treatment resulting in larger aerosol particles), meaning that derived parameters such as the AOD at 870 nm or the Ångström exponent between these two wavelengths are also more diverse. This is an indication of the sensitivity of aerosol retrieval algorithms to assumptions about surface reflectance. Fig. 8 reveals that the average decrease in 550 nm AOD of 0.032 upon adoption of the SVD-based scheme applies over many regions of the world aside from the rainforests of Amazonia, central Africa, and Borneo (where the change is of similar magnitude but positive), Australia (where the difference is, again, positive) and arid regions through northern Africa and southern/central Asia (more strongly negative).

Over a large ensemble of retrievals, the distribution of retrieval cost is expected to approximate a χ^2 distribution with 1.5 degrees of freedom (Sayer et al., 2010). Fig. 9 shows this theoretical distribution, along with the observed distributions from the SVD and unadjusted retrieval runs. The SVD adjustment results in a closer agreement with the theoretical distribution, although the higher-than-expected proportion of retrievals with cost under 5 suggests that the uncertainties comprising $\mathbf{S}_y$ and $\mathbf{S}_x$ may be overestimated in some cases.

Fig. 10 shows the number of successful retrievals, mean number of iterations, and mean cost for both runs. Particularly over deserts and
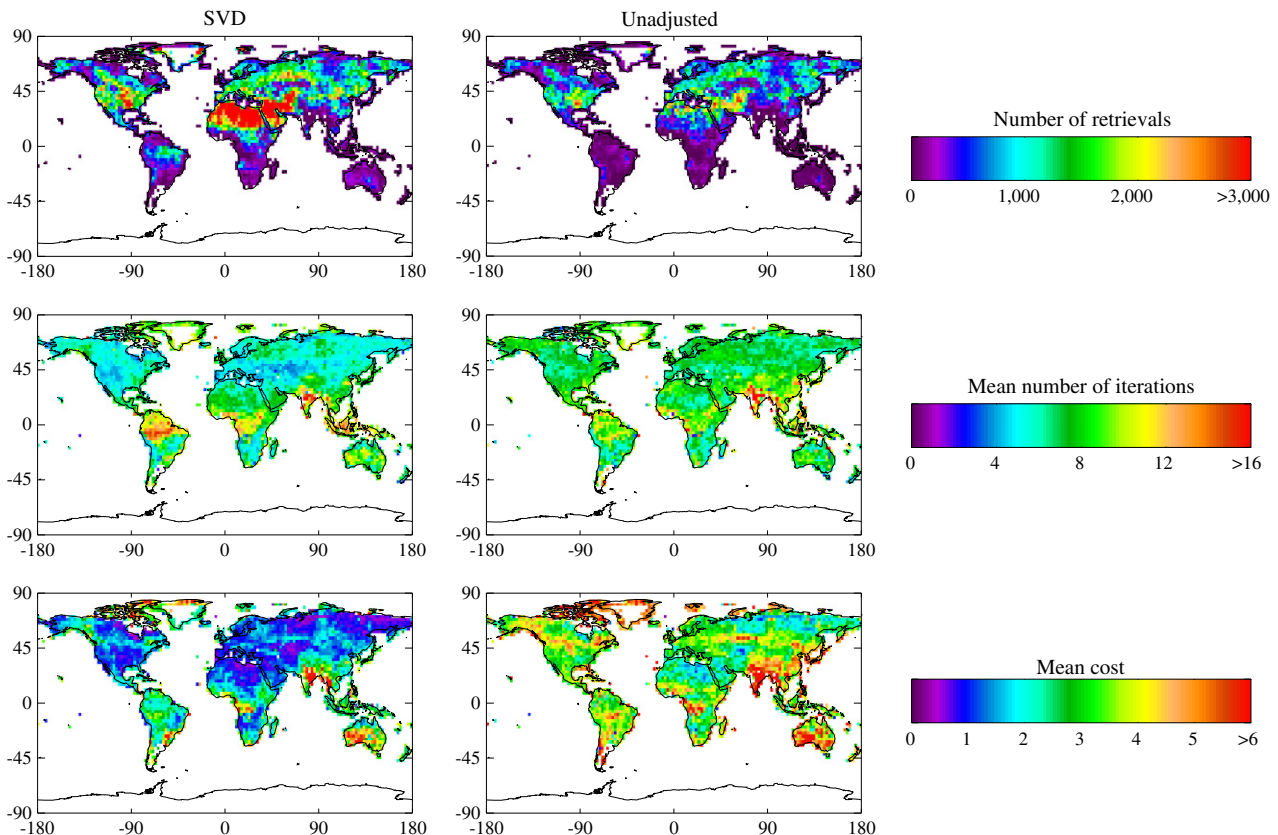
Fig. 10. Monthly mean retrieval statistics for the SVD (left) and unadjusted surface (right) runs on a 2.5° grid. From top to bottom, the maps show the total number of successful retrievals, the mean number of iterations needed before convergence, and the mean cost of successful retrievals.

Table 4
Comparison between AATSR and AERONET 550 nm AOD using the new SVD-based land surface reflectance ('SVD') treatment with the previous land surface reflectance treatment ('unadjusted'). RMS indicates the root mean square difference.

Surface treatment	Correlation coefficient r	RMS difference	Mean difference (AATSR-AERONET)	Mean absolute difference
Unadjusted	0.510	0.141	0.011	0.088
SVD	0.539	0.136	− 0.002	0.085

Amazonia, the new SVD treatment results in a notably larger number of successful retrievals. Convergence is also generally faster, and the average cost is decreased globally, although there remains regional variability (which may be due to differences in regional quality of the MCD43B1 product, aerosol model assumptions, or cloud screening).

The Aerosol Robotic Network (AERONET, Holben et al., 1998) provides ground-based aerosol data against which the retrieved 550 nm AOD can be validated. For this comparison, both sets of AATSR retrievals have been aggregated to a 0.5° grid on a daily basis. Level 2.0 (cloud-screened and quality assured) AERONET data have been averaged for each station to create daily means and the AATSR grid cell in which they lie identified. The AERONET AOD at 550 nm is obtained from the AOD provided at 500 nm and the Ångström exponent between 500 nm and 870 nm. The resulting datasets are then compared where both indicate a well-sampled, reasonably homogeneous scene (at least 5 AATSR retrievals and AERONET measurements, and standard deviations of AOD smaller than 0.2). For July 2008 there are 133 coincidences where all three datasets meet this criterion.

Comparative statistics for these coincidences are provided in Table 4. The SVD-based surface treatment results in an improved comparison, although the improvement is small, suggesting that the main benefit of this scheme is the increased number of successful retrievals and decreased retrieval cost. Overall, for the SVD-based surface treatment 62% of the differences between AERONET and AATSR AOD are smaller than $0.05 + 15\%$, and 44% are within $0.03 + 10\%$. For the previous unadjusted surface treatment, these figures are 59% and 42% respectively.

6. Summary

Convolving high-resolution surface spectra with the spectral response functions of similar AATSR and MODIS channels reveals differences between the apparent surface albedo measured by each sensor. These differences are typically 0.001–0.01, dependent on wavelength and surface type. The ORAC aerosol retrieval for AATSR uses MODIS-derived BRDF model parameters to constrain the surface reflectance and so these differences introduce a source of error which may impact upon the quality of aerosol retrievals, as these are sensitive to assumptions about surface reflectance. Singular value decomposition using the high-resolution surface spectra as a training dataset reduces these errors and effectively removes the biases. The error budget of the aerosol retrieval relating to the surface reflectance has also been improved. The technique described has other potential applications, and could for example be used as a tool to combine surface reflectance datasets derived from multiple sensors in a consistent way.

Application of the improved algorithm to a month of AATSR data reveals that for almost all land locations it increases the number of successful retrievals, and improves the level of consistency between the measurements and the retrieved state. Retrieved AOD at 550 nm shows a small improvement in correspondence when compared to AERONET data. These results provide confidence that the new algorithm represents an improvement, although there is scope for further refinement of aerosol models, surface reflectance, cloud

flagging and forward model error to improve performance in some regions.

References

Baldridge, A. M., Hook, S. J., Grove, C. I., & Rivera, G. (2009). The ASTER spectral library version 2.0. *Remote Sensing of Environment*, *113*, 711–715 Spectra available online at. http://speclib.jpl.nasa.gov/ [Accessed August 2010].

Clark, R. N., Swayze, G. A., Wise, R., Livo, K. E., Hoefen, T. M., Kokaly, R. F., et al. (2003). USGS Digital Spectral Library splib05a. *USGS Open File Report 03-395* http://pubs.usgs.gov/of/2003/ofr-03-395/ofr-03-395.html [Accessed August 2010].

Diner, D., Martonchik, J. V., & Kahn, R. (2005). Using angular and spectral shape similarity constraints to improve MISR aerosol and surface retrievals over land. *Remote Sensing of Environment*, *94*, 155–171.

Dubovik, O., Holben, B., Eck, T. F., Smirnov, A., Kaufman, Y., Kind, M., et al. (2002). Variability and optical properties of key aerosol types observed in worldwide locations. *Journal of the Atmospheric Sciences*, *59*, 590–608.

Forster, P., Ramaswamy, V., Artaxo, P., Berntsen, T., Betts, R., Fahey, D. W., et al. (2007). Changes in atmospheric constituents and in radiative forcing. *Climate Change 2007, the physical science basis. Contribution of Working Group 1 to the fourth assessment report of the Intergovernmental Panel on Climate Change* : Cambridge University Press.

Hasekamp, O. P., & Landgraf, J. (2007). Retrieval of aerosol properties over land surfaces: Capabilities of multi-viewing-angle intensity and polarization measurements. *Applied Optics*, *46*, 3332–3344.

Hess, M., Koepke, P., & Schult, I. (1998). Optical properties of aerosols and clouds: The software package OPAC. *Bulletins of the American Meteorological Society*, *79*, 831–944.

Holben, B. N., Eck, T. F., Slutsker, I., Tanré, D., Buis, J. P., Setzer, A., et al. (1998). AERONET: A federated instrument network and data archive for aerosol characterization. *Remote Sensing of Environment*, *66*, 1–16.

Hsu, N. C., Tsay, S. -C., King, M. D., & Herman, J. R. (2004). Aerosol properties over bright-reflecting source regions. *IEEE Transactions on Geoscience and Remote Sensing*, *42*, 557–569.

Istomina, L. G., von Hoyningen-Huene, W., Kokhanovsky, A. A., & Burrows, J. P. (2010). The detection of cloud-free snow-covered areas using AATSR measurements. *Atmospheric Measurement Techniques*, *3*, 1005–1017.

Jin, Y., Schaaf, C. B., Woodcock, C. E., Gao, F., Li, X., Strahler, A. H., et al. (2003a). Consistency of MODIS surface bidirectional reflectance distribution function and albedo retrievals: 1. Algorithm performance. *Journal of Geophysical Research*, *108* (D5).

Jin, Y., Schaaf, C. B., Woodcock, C. E., Gao, F., Li, X., Strahler, A. H., et al. (2003b). Consistency of MODIS surface bidirectional reflectance distribution function and albedo retrievals: 2. Validation. *Journal of Geophysical Research*, *108*(D5).

Kandler, K., Benker, N., Bundke, U., Cuevas, E., Ebert, M., Knippertz, P., et al. (2007). Chemical composition and complex refractive index of Saharan Mineral Dust at Izana, Tenerife (Spain) derived by electron microscopy. *Atmospheric Environment*, *41*, 8058–8074.

Kokhanovsky, A., Bréon, F. -M., Cacciari, A., Carboni, E., Diner, D., Di Nicolantonio, W., et al. (2007). Aerosol remote sensing over land: A comparison of satellite retrievals using different algorithms and instruments. *Atmospheric Research*, *85*, 372–394.

Kokhanovsky, A. A., Deuzé, J. L., Diner, D. J., Dubovik, O., Ducos, F., Emde, C., et al. (2010). The inter-comparison of major satellite aerosol retrieval algorithms using simulated intensity and polarization characteristics of reflected light. *Atmospheric Measurement Techniques*, *3*, 909–932.

Levy, R. C., Remer, L. A., Mattoo, S., Vermote, E. F., & Kaufman, Y. J. (2007). Second-generation operational algorithm: Retrieval of aerosol properties over land from inversion of Moderate Resolution Imaging Spectroradiometer spectral reflectance. *Journal of Geophysical Research*, *112*.

Liu, J., Schaaf, C., Strahler, A., Jiao, Z., Shuai, Y., Zhang, Q., et al. (2009). Validation of Moderate Resolution Imaging Spectroradiometer (MODIS) albedo retrieval algorithm: Dependence of albedo on solar zenith angle. *Journal of Geophysical Research*, *114*.

Lucht, W., Schaaf, C. B., & Strahler, A. H. (2000). An algorithm for the retrieval of albedo from space using semiempirical BRDF models. *IEEE Transactions on Geoscience and Remote Sensing, 38*, 977–998.

Martonchik, J. V., Diner, D. J., Kahn, R. A., Ackerman, T. P., Verstraete, M. M., Pinty, B., et al. (1998). Techniques for the retrieval of aerosol properties over land and ocean using multiangle imaging. *IEEE Transactions on Geoscience and Remote Sensing, 36*, 1212–1227.

Mishchenko, M. I., & Travis, L. D. (1998). Capabilities and limitations of a current FORTRAN implementation of the T-matrix method for randomly oriented, rotationally symmetric scatterers. *Journal of Quantitative Spectroscopy and Radiative Transfer, 60*, 309–324.

North, P. R. (2002). Estimation of aerosol opacity and land surface bidirectional reflectance from ATSR-2 dual-angle imagery: Operational method and validation. *Journal of Geophysical Research, 107*.

Rodgers, C. D. (2000). Inverse methods for atmospheric sounding: Theory and practice. *Series on Atmospheric, Oceanic and Planetary Physics, Vol. 2*: World Scientific.

Saloman, J. G., Schaaf, C. B., Strahler, A. H., Gao, F., & Jin, Y. (2006). Validation of the MODIS bidirectional reflectance distribution function and albedo retrievals using combined observations from the Aqua and Terra platforms. *IEEE Transactions on Geoscience and Remote Sensing, 44*, 1555–1565.

Sayer, A. M. (2009). *Aerosol remote sensing using AATSR.* Ph.D. thesis University of Oxford. Available online at http://www.atm.ox.ac.uk/group/eodg/theses/Sayer.pdf

Sayer, A. M., Thomas, G. E., & Grainger, R. G. (2010). A sea surface reflectance model for (A)ATSR, and application to aerosol retrievals. *Atmospheric Measurement Techniques, 3*, 813–838.

Schaaf, C. B., Gao, F., Strahler, A. H., Lucht, W., Li, X., Tsang, T., et al. (2002). First operational BRDF, albedo nadir reflectance products from MODIS. *Remote Sensing of Environment, 83*, 135–148.

Schaepman-Strub, G., Schaepman, M. E., Painter, T. H., Dangel, S., & Martonchik, J. V. (2006). Reflectance quantities in optical remote sensing—Definitions and case studies. *Remote Sensing of Environment, 103*, 27–42.

Shuai, Y., Schaaf, C. B., Strahler, A. H., Liu, J., & Jiao, Z. (2010). Quality assessment of BRDF/albedo retrievals in MODIS operational system. *Geophysical Research Letters, 35*.

Smith, D., Poulsen, C., & Latter, B. (2008). Calibration status of the AATSR reflectance channels. *2008 ESA MERIS/(A)ATSR Workshop SP-666*.

Stevens, B., & Feingold, G. (2009). Untangling aerosol effects on clouds and precipitation in a buffered system. *Nature, 461*, 607–613.

Thomas, G. E., Poulsen, C. A., Sayer, A. M., Marsh, S. H., Dean, S. M., Carboni, E., et al. (2009a). Oxford-RAL Aerosol and Cloud (ORAC): Aerosol retrievals from satellite radiometers. In A. A. Kokhanvosky, & G. de Leeuw (Eds.), *Satellite Aerosol Remote Sensing Over Land*. Berlin: Springer.

Thomas, G. E., Poulsen, C. A., Sayer, A. M., Marsh, S. H., Dean, S. M., Carboni, E., et al. (2009b). The GRAPE aerosol retrieval algorithm. *Atmospheric Measurement Techniques, 2*, 679–701.

Torres, O., Bhartia, P. K., Herman, J. R., & Ahmad, Z. (1998). Derivation of aerosol properties from satellite measurements of backscattered ultraviolet radiation: Theoretical basis. *Journal of Geophysical Research, 103*, 17099–17110.

Veefkind, J. P., de Leeuw, G., & Durkee, P. A. (1998). Retrieval of aerosol optical depth over land using two-angle view satellite radiometry during TARFOX. *Geophysical Research Letters, 25*, 3135–3138.

von Hoyningen-Huene, W., Freitag, M., & Burrows, J. P. (2002). Retrieval of spectral aerosol optical thickness from multi-wavelength space-borne sensors. *Advances in Space Research, 49*, 1765–1770.

von Hoyningen-Huene, W., Freitag, M., & Burrows, J. P. (2003). Retrieval of aerosol optical thickness over land surfaces from top-of-atmosphere radiance. *Journal of Geophysical Research, 108*(D9).

Wanner, W., Li, X., & Strahler, A. H. (1995). On the derivation of kernels for kernel-driven models of bidirectional reflectance. *Journal of Geophysical Research, 100*, 21077–21089.

Wanner, W., Strahler, A., Hu, B., Lewis, P., Muller, J., Li, X., et al. (1997). Global retrieval of bidirectional reflectance and albedo over land from EOS MODIS and MISR data: Theory and algorithm. *Journal of Geophysical Research, 102*, 17143–17161.

Ward, H. (2009). *Temporal variability of surface albedo.* MPhys project report, Atmospheric, Oceanic and Planetary Physics, Department of Physics, University of Oxford Available online at http://www.atm.ox.ac.uk/group/eodg/mphys_reports/2009_Ward.pdf